ADVANCED MATERIALS
www.advmat.de

Atomic-Precision Repair of a Few-Layer 2H-$MoTe_2$ Thin Film by Phase Transition and Recrystallization Induced by a Heterophase Interface

Xiaolong Xu, Bo Han, Shuai Liu, Shiqi Yang, Xionghui Jia, Wanjin Xu, Peng Gao, Yu Ye, and Lun Dai**

2D semiconductors have emerged as promising candidates for post-silicon nanoelectronics, owing to their unique properties and atomic thickness. However, in the handling of 2D material, various forms of macroscopic damage, such as cracks, wrinkles, and scratches, etc., are usually introduced, which cause adverse effects on the material properties and device performance. Repairing such macroscopic damage is crucial for improving device performance and reliability, especially for large-scale 2D device arrays. Here, a method is demonstrated repair damage to few-layer 2H-$MoTe_2$ films with atomic precision, and its mechanism is elucidated. The repaired 2H-$MoTe_2$ inherits the lattice orientation of the adjacent original 2H-$MoTe_2$, thereby forming an atomically perfect lattice at the repaired interface. The time-evolution experiments show that the interface between the 2H- and early formed 1T'-$MoTe_2$ plays an important role in the subsequent phase transition and recrystallization. Electrical measurements on the original $MoTe_2$, repaired $MoTe_2$, and cross-interface regions show unobservable differences, indicating that the repaired $MoTe_2$ has the same electrical quality as the original one and the interface does not introduce extra scattering centers for carrier transport. The findings provide an effective strategy for macroscopic damage repair of few-layer 2H-$MoTe_2$, which paves the way for its practical application in advanced electronics and optoelectronics.

X. Xu, S. Liu, S. Yang, X. Jia, Dr. W. Xu, Prof. Y. Ye, Prof. L. Dai
State Key Laboratory for Artificial Microstructure
and Mesoscopic Physics and Frontiers Science Center for
Nano-Optoelectronics
School of Physics
Peking University
Beijing 100871, China
E-mail: ye_yu@pku.edu.cn; lundai@pku.edu.cn

B. Han, Prof. P. Gao
Electron Microscopy Laboratory and International Center
for Quantum Materials
School of Physics
Peking University
Beijing 100871, China

S. Yang
Academy for Advanced Interdisciplinary Studies
Peking University
Beijing 100871, China

Prof. P. Gao, Prof. Y. Ye, Prof. L. Dai
Collaborative Innovation Center of Quantum Matter
Beijing 100871, China

The ORCID identification number(s) for the author(s) of this article can be found under https://doi.org/10.1002/adma.202000236.

DOI: 10.1002/adma.202000236

Atomically thin 2D materials have attracted wide interest in scientific research and electronic/optoelectronic device applications.[1–6] Novel physical phenomena, such as valley-related effects,[7,8] and Moiré physics, etc., have been reported.[9–11] 2D transition metal dichalcogenides (TMDCs) have emerged as promising candidates for postsilicon nanoelectronic technology, due to their unique semiconducting properties and atomic thicknesses. On the way to implementing 2D materials for monolithic integration technology, high device yield, and reliability are critical. Among the Mo- and W-based 2D TMDCs, $MoTe_2$ is particularly interesting because of the small free energy difference between the semiconducting 2H phase and metallic 1T' phase.[12] This small energy difference (≈40 meV per $MoTe_2$ formula unit) leads to the possibility of phase controlled synthesis of $MoTe_2$ film. The large-scale semiconducting 2H-$MoTe_2$ with single-crystalline domain size up to hundreds of micrometer has been synthesized by the unique phase transition between 1T'- to 2H-$MoTe_2$.[13] Due to the moderate bandgap of few-layer 2H-$MoTe_2$ of 1.0 eV, ambipolar charge transport[14] and optical devices operated at standardized telecom wavelengths[15] have been reported using $MoTe_2$. Monolithic integration allows both the electronics and the optical devices to be integrated with van der Waals $MoTe_2$ in a single growth process. However, in the processes of 2D material synthesis and device fabrication, especially in the process of material transfer (a common and key step in the 2D device fabrication process), various forms of macroscopic damage, such as cracks, wrinkles, holes, and scratches, etc., are usually introduced, which will adversely affect the device performance and directly increase the chip failure risk.[16,17] Minimizing or repairing such macroscopic damage is essential to improve device performance and reliability, especially for large-scale 2D device arrays. So far, various methods have been developed to repair microscopic damage (e.g., defects, nanopores, etc.) in 2D materials, including vapor deposition,[18] electron beam irradiation,[19] chemical doping,[20] etc. However, to the best of our knowledge, no effective method of repairing the macroscopic damage in 2D materials was reported. Here, we demonstrate a method to precisely repair the macroscopic damage to few-layer

2H-$MoTe_2$ film at the atomic scale, and elucidate the repair mechanism. High-angle annular dark-field scanning transmission electron microscopy (HAADF-STEM) is used to resolve the in-plane atomic arrangements at the repaired interface, where an atomically perfect lattice is observed. Electron back-scattered diffraction (EBSD) characterizations show that the repaired 2H-$MoTe_2$ inherits the lattice orientation of the adjacent original 2H-$MoTe_2$ domain. In order to study the repair mechanism, we conduct time-evolution experiments, which shows that 1T'-$MoTe_2$ is formed at an early stage, and the interface between the 2H and 1T'-$MoTe_2$ plays an important role in the subsequent phase transition and recrystallization. The repaired $MoTe_2$ film shows no significant difference in electrical properties from the original $MoTe_2$, and due to the atomic precision repair, the interface between the original and repaired $MoTe_2$ does not introduce additional scattering centers for carrier transport. This novel and effective macroscopic damage repair strategy paves the way for the practical application of 2D materials in advanced electronics and optoelectronics.

First, a large-scale few-layer 2H-$MoTe_2$ film was synthesized by tellurizing a 7 nm sputtered Mo film (650 °C for 2 h) on a p^+-Si/SiO_2 substrate via the chemical vapor deposition (CVD) method.[13,21–23] The as-synthesized $MoTe_2$ was about 10 nm thick (Figure S1, Supporting Information), corresponding to a 14-layer film. It is worth noting that the thickness of the $MoTe_2$ film can be easily tuned by controlling the thickness of the deposited Mo film.

To demonstrate the macroscopic damage repair method, we intentionally scratched the 2H-$MoTe_2$ film (**Figure 1**a,e). The detailed repair process is schematically illustrated in Figure 1a–d. First, photolithography was used to define a window that covered the damaged area. Subsequently, a reactive ion etching (RIE) process was employed to remove the 2H-$MoTe_2$ in the window, leaving a bare substrate in the window area. Then, a 7 nm thick Mo film was deposited in this window by magnetron sputtering, followed by a lift-off process (Figure 1b,f). Finally, the sample was sent back into the furnace for tellurizing at 650 °C for 30 min (Figure 1d). After the repair, we can see uniform optical contrast across the whole 2H-$MoTe_2$ film (Figure 1h). The original 2H-$MoTe_2$ was synthesized under the same condition of the repair process and remained unaffected during the repair process. This was confirmed by the unaffected out-of-plane A_{1g} (171 cm^{-1}) and the strong in-plane E^1_{2g} (234 cm^{-1}) Raman modes of 2H-$MoTe_2$ (Figure S2, Supporting Information).[24,25] The Raman spectroscopy mapping of the 2H-$MoTe_2$'s representative fingerprint, E^1_{2g} mode (Figure 1k), showed a uniform integrated intensity (labeled by the corresponding dashed lines in Figure 1i) at the interface (labeled by the black dashed box in Figure 1h), confirming that the repaired region was 2H-$MoTe_2$. To unravel the repair mechanism, we performed a time evolution study. In a short tellurizing time of 2 min, only 1T'-$MoTe_2$ was formed in the area to be repaired (Figure 1c), which was confirmed by the appearance of the well-resolved A_g Raman modes (76, 107, 161, and 256 cm^{-1}) of 1T'-$MoTe_2$ (Figure 1i).[26–28] Due to

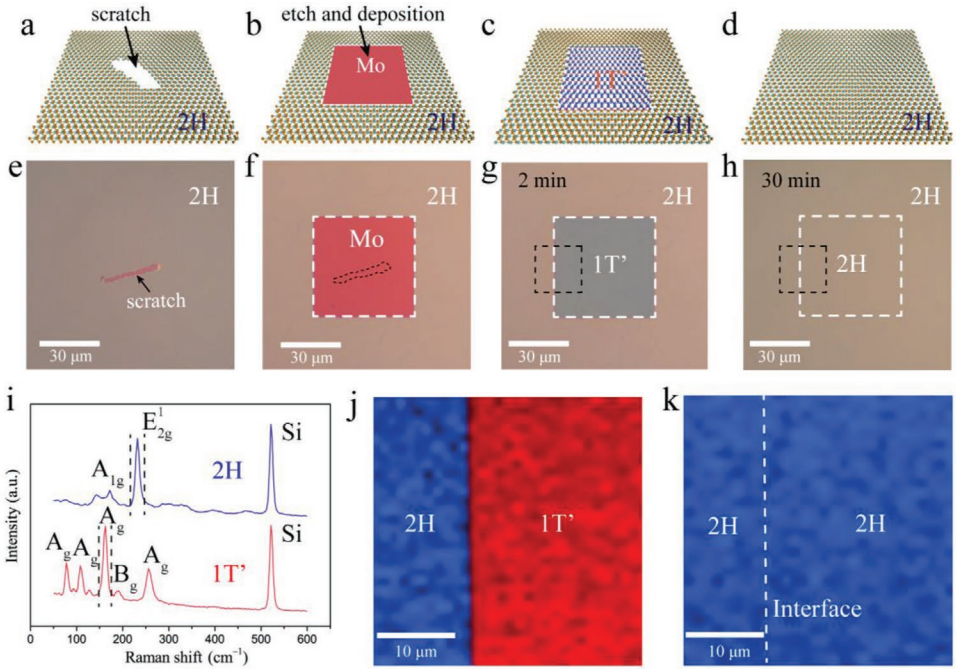

Figure 1. Repair processes and Raman characterizations. a–h) Schematic illustrations and corresponding optical images of the repair processes. a,e) A 2H-$MoTe_2$ film with a scratch. b,f) A window was defined to cover the damaged area by UV lithography, followed by a reactive ion etching (RIE) process. A 7 nm Mo film was deposited in the window by magnetron sputtering followed by a lift-off process. c,g) After removing the photoresist, the sample was sent back into the furnace at 650 °C for tellurizing. In a short tellurizing time of 2 min, the Mo thin film was fully tellurized into 1T'-$MoTe_2$, which shows obvious optical contrast with that of 2H-$MoTe_2$. d,h) As the tellurizing time increased to 30 min, the 1T'-$MoTe_2$ was fully phase-transformed into 2H-$MoTe_2$, and the optical contrast across the whole $MoTe_2$ film is uniform. i) Raman spectra measured at 2H- and 1T'-$MoTe_2$ regions shown in (g). The well-resolved Raman signatures of 1T'-$MoTe_2$ confirm that the Mo thin film was fully tellurized into 1T'-$MoTe_2$ in a 2 min tellurizing process. j) Raman mapping image of E^1_{2g} mode of 2H-$MoTe_2$ and A_g mode of the 1T'-$MoTe_2$ at the interface of the 2 min tellurized film (labeled by the black dashed box in (g)). k) Raman mapping image of E^1_{2g} mode of 2H-$MoTe_2$ at the interface of the 30 min repaired film (labeled by the black dashed box in (h)).

the significant dielectric constant different between the semiconducting 2H-$MoTe_2$ and metallic 1T'-$MoTe_2$, there was a large optical contrast difference between the original 2H-$MoTe_2$ and the formed 1T'-$MoTe_2$ (Figure 1g). The Raman spectroscopy mapping (Figure 1j) of the representative fingerprints A_g mode of 1T'-$MoTe_2$ and E^1_{2g} mode of 2H-$MoTe_2$ (labeled by the corresponding dashed lines in Figure 1i) at the interface (labeled by the black dashed box in Figure 1g) showed a clear demarcation between the 1T'- and 2H-$MoTe_2$ (see the separated intensity contrast in Figure S3, Supporting Information). During the repairing process, the interface between 1T' and 2H $MoTe_2$ plays an important role. The tellurium and molybdenum atoms in the 1T' phase will cross the interface into the 2H-$MoTe_2$ and rearrange themselves to copy the lattice of the adjacent 2H-$MoTe_2$ (discussed later). At an intermediate tellurizing time of 5 min, the interface of 1T'/2H $MoTe_2$ is pushed inward to the 1T' region from the four sides of the square region, and a new 1T'/2H $MoTe_2$ interface with a smaller size is created (Figure S4, Supporting Information). Due to the different phase transition rates on the four sides, the irregular shapes of the new 1T'/2H-$MoTe_2$ interfaces are often observed (Figure S4, Supporting Information). The interface of the 1T'/2H-$MoTe_2$ disappears until the phase transition and recrystallization process is completed after a long enough tellurizing time (Figure 1d,h).

To further verify the repair mechanism, we employed scanning transmission electron microscopy (STEM) to characterize the interfaces at different stages of the repair process. The early formed 2H-1T' heterophase film and the fully repaired 2H-$MoTe_2$ film were transferred onto the copper grids. At the 2H-1T' heterophase interface, the HAADF-STEM image (**Figure 2**b) showed that 1T'-$MoTe_2$ and 2H-$MoTe_2$ were seamlessly stitched, forming an atomically smooth interface. The corresponding fast Fourier transform (FFT) patterns of the 2H phase domain and the 1T' phase domain are shown in Figure S5a,b (Supporting Information), which contain a set of hexagonal 2H spots and a set of monoclinic 1T' spots, respectively.[29] Our previous study indicates that the 2H-$MoTe_2$ single-crystalline domain can be as large as hundreds of micrometers, while the 1T'-$MoTe_2$ domain is of about tens of nanometers.[13] The selected area electron diffraction (SAED) pattern (Figure 2c) obtained at the interface with an aperture size of 800 nm comprises a single set of sixfold symmetric diffraction spots related to single-crystalline 2H-$MoTe_2$, and a series of diffraction rings related to polycrystalline 1T'-$MoTe_2$.[2,29,30] The HAADF-STEM image at the fully repaired 2H-$MoTe_2$ interface shows a perfect lattice without any crystal angular deflection and grain boundaries (Figure 2e), indicating that 1T'-$MoTe_2$ has been completely transformed into 2H-$MoTe_2$. In addition, the SAED pattern obtained at the interface with an aperture size of 800 nm comprises only one set of hexagonal 2H spots (Figure 2d), indicating the repaired 2H-$MoTe_2$ film inherits the lattice orientation of the originally attached 2H-$MoTe_2$. It is worth noting that the 1T'/2H interface formed at the early stage plays an important role in the repair process. Once the 1T'/2H interface is formed, as the growth proceeds, the Te and Mo atoms in the metastable 1T'-$MoTe_2$ will migrate and rearrange themselves according to the lattice structure and orientation of the adjacent 2H-$MoTe_2$ (Figure 2a), and finally, phase transforms to 2H-$MoTe_2$. The migration and rearrangement of these atoms lead to an atomically smooth repair of the macroscopic damage of the 2H-$MoTe_2$ film.

To find the crystal orientation of the repaired 2H-$MoTe_2$ film on a larger scale, we used a scanning electron microscope (SEM) equipped with EBSD to characterize the interface of the repaired film. Two typical cases were investigated: one containing multiple domains and the other containing a single domain in the original 2H-$MoTe_2$ region. A slight contrast difference can be observed in the band contrast images between the original region and the repaired region (**Figure** 3a,d), due to the small thickness difference (herein, the thickness of the Mo film used to

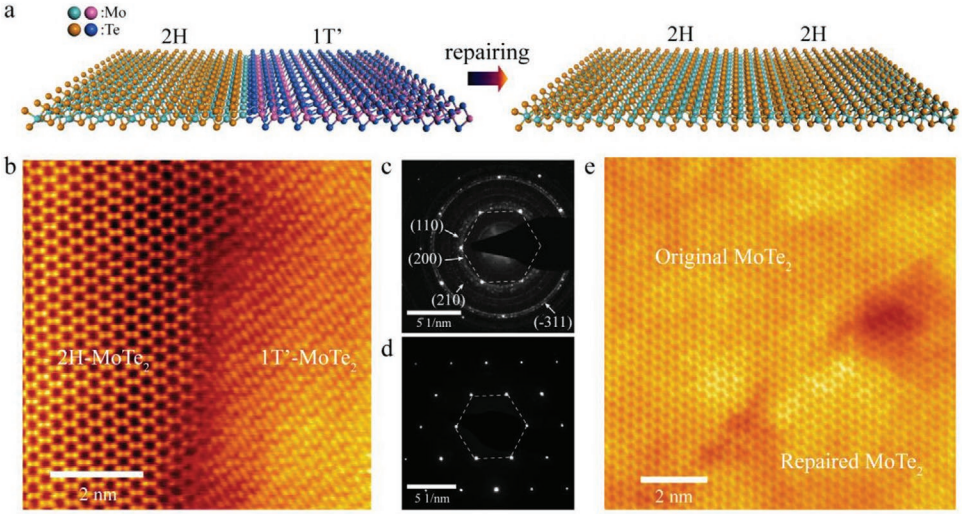

Figure 2. TEM characterizations of the repaired interfaces. a) Schematic illustrations of the repair mechanism. 1T'-$MoTe_2$ is formed early in the area to be repaired, and phase transforms into 2H-$MoTe_2$ as the growth proceeds. b) A representative HAADF-STEM image of a 1T'/2H $MoTe_2$ interface formed at the early stage, where an atomically smooth interface is observed. c) SAED pattern of the 1T'/2H $MoTe_2$ interface, which comprises a single set of diffraction spots with sixfold symmetry related to the single-crystalline 2H-$MoTe_2$ and a series of diffraction rings related to the polycrystalline 1T'-$MoTe_2$. d) SAED pattern of the fully repaired 2H-$MoTe_2$ interface. Only one set of hexagonal 2H phase spots is observed. e) HAADF-STEM image of the fully repaired 2H-$MoTe_2$ interface, showing a perfect lattice arrangement without any crystal angular deflection and grain boundaries.

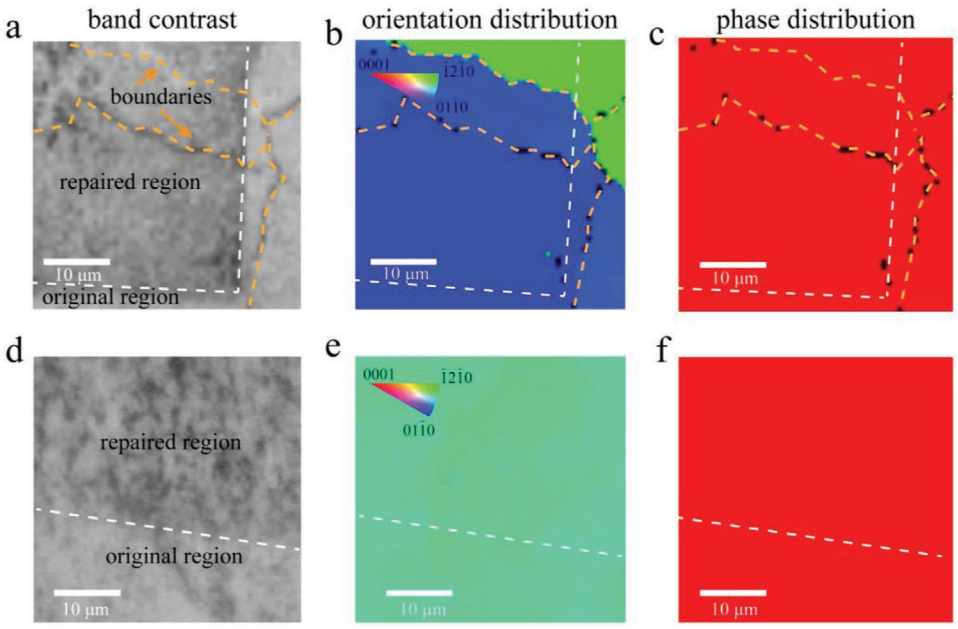

Figure 3. EBSD characterizations of the fully repaired 2H-$MoTe_2$ film near the interface. a,d) Band contrast images taken at the interfaces with multiple domains and single domain in the original 2H-$MoTe_2$, respectively. The domain boundaries are marked by the orange dashed lines. The repaired interfaces are marked by the white dashed lines. To distinguish the interface under the SEM, a small thickness difference between the original and repaired $MoTe_2$ was intentionally created. b,e) The EBSD mapping images along the x-axis direction near the interfaces with multiple domains and a single domain in the original 2H-$MoTe_2$, respectively. The repaired region inherits the crystal orientation of its adhered original domain. c,f) Phase distributions at the interfaces. The uniform colors were indicative of the complete phase transition during the repair process.

synthesize the repaired region is about 6 nm), which was intentionally controlled to locate the interface under the SEM (marked by the white dashed lines). Grain boundaries can also be distinguished in the band contrast image (Figure 3a, marked by the orange dashed lines). From the EBSD orientation mapping along the x-axis direction at the repaired interface with multiple crystal domains (Figure 3b), the grain boundaries continue to extend from the original region to the repaired region. The grain boundaries divide the repaired film into different crystal domains, and each domain has the same lattice orientation as its adjacent original crystal domains, which is in good agreement with the STEM results. The inheritance of the adjacent original crystal orientation was further confirmed by the Kikuchi patterns (Figure S6, Supporting Information). Again, these results can be understood as that the repair process starts from the early formed 1T'/2H $MoTe_2$ interface, and then extends to the region to be repaired through the 1T' to 2H phase transition. For the single original domain case (Figure 3d), the EBSD orientation mapping along the x-axis direction showed a uniform color without any grain boundaries (Figure 3e), indicating the single-crystalline nature of the fully repaired film. It is worth noting that this atomically smooth repair method does not leave any "scars" at the interface, which is particularly important for repairing a 2D single crystal. In addition, in both cases, the EBSD mapping images along the z-axis direction showed uniform colors (Figure S7, Supporting Information), indicating that 2H-$MoTe_2$ thin films stack layer by layer along the direction perpendicular to the substrate. Besides, in both cases, the phase distributions showed uniform colors (Figure 3c,f), indicating that the phase transition in the repair process was thorough, which was also proved by the Raman mapping results (Figure 1k).

Finally, we evaluated the electrical properties of the $MoTe_2$ film after the repair process. A rectangular 2H-$MoTe_2$ channel with a channel width of 15 μm was fabricated by UV photolithography, followed by an RIE process. There were three representative regions on the $MoTe_2$ channel: the original region, the repaired region, and the cross-interface region. Six equally separated electrodes (10/50 nm Pd/Au) with a spacing of 10 μm were fabricated on the $MoTe_2$ channel by UV photolithography, metallization, and lift-off processes. The electrical properties of these three different regions were characterized by measuring the corresponding field-effect transistor (FET) performance (**Figure 4**a), using the p^+-silicon as the gate electrode. Under a source–drain bias voltage of 0.5 V, all transfer curves overlap with each other, showing p-type channel characteristics with an on-off ratio of $\approx 1 \times 10^3$ (Figure 4b). The room-temperature field-effect mobilities (μ) were measured to be 3.1, 3.4, and 3.2 $cm^2\ V^{-1}\ s^{-1}$, for the original region, repaired region, and cross-interface region, respectively, using $\mu = (dI_{ds}/dV_g)\ (L/W)\ (1/V_{ds}C_g)$, where L, W, and C_g are the channel length, channel width, and the gate capacitance per unit area, respectively. The field-effect performance of these three different regions was also similar to that of the FET made on the pristine 2H-$MoTe_2$ without the repair process (Figure S8a,b, Supporting Information), which suggests that the electrical properties of the material were not affected during this repair process. Moreover, the resistances of these three regions were measured by a four-probe method, in which the contact resistance was eliminated. The resistances of these three regions under zero back-gate voltage were almost identical to each other (Figure 4c), and also identical

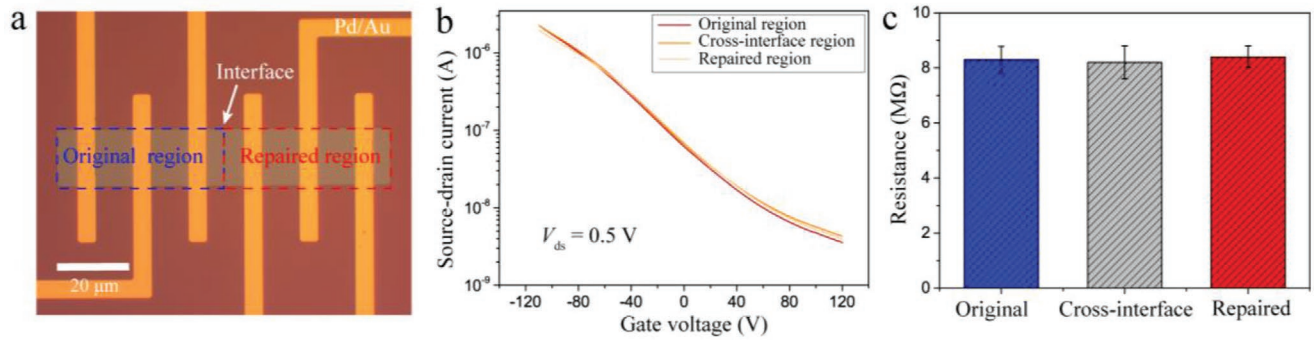

Figure 4. Electrical characterizations of the repaired 2H-$MoTe_2$ film. a) Optical image of the device. Six equally separated electrodes (10/50 nm Pd/Au) were fabricated on three typical regions in such a way that we can characterize the electrical properties of the three different regions: original region, cross-interface region, and repaired region. b) The transfer curves of the three representative FETs under a source–drain bias voltage of 0.5 V. The room-temperature performances of these three different FETs are similar, which are also similar to that of the FET made on a pristine 2H-$MoTe_2$, suggesting that the material's electrical properties are preserved after the repair process. c) Resistances of these three different regions measured by the four-probe method. The error bar is calculated by measuring three different devices with identical geometry. The results show that the resistances in the three different regions are almost the same.

to that of a pristine 2H-$MoTe_2$ (Figure S8c, Supporting Information). This again indicates that the repaired $MoTe_2$ has the same electrical quality as the original $MoTe_2$, and no additional scattering centers for carrier transport are introduced by the interface between the original and repaired $MoTe_2$, which could be essentially important for repairing integrated electronics.

In summary, we demonstrate a method to precisely repair macroscopic damage of a few-layer 2H-$MoTe_2$ film at the atomic scale, and elucidate the repair mechanism. Raman spectroscopy, HAADF-STEM, and EBSD, etc. are employed to characterize the repair results. Through the time-evolution experiments, we find that the interface between 2H- and 1T'-$MoTe_2$ formed at the early stage plays an important role in the repair process, thereby ensuring the subsequent phase transition and recrystallization process. Once the 1T'/2H interface is formed, the Te and Mo atoms in the 1T'-$MoTe_2$ will migrate and rearrange themselves according to the lattice structure of the adjacent 2H-$MoTe_2$ domain. As a result, the repaired region will inherit the lattice structure and orientation of the adjacent original 2H-$MoTe_2$ domain. We also demonstrate that the repaired $MoTe_2$ has the same electrical quality as the original $MoTe_2$, and the repaired interfaces do not introduce additional scattering centers for electrical transport due to the atomic precision repair. Until now, applying this method to other TMDCs still requires more effort. This is because the energy difference between the 2H phase and 1T' (or 1T) phase of other TMDCs are much larger than that of the $MoTe_2$, which hinder the phase transition and recrystallization in the growth process. But big strides have been made in the growth of stable 1T' (or 1T) phase of other TMDCs. For example, the stable 1T' phase of MoS_2 has been synthesized directly based on the CVD method by choosing the proper precursor.[31] With the development of phase engineering in TMDCs, it is possible to repair other TMDCs materials by similar methods. Our findings demonstrate a novel and effective strategy for repairing macroscopic damage to few-layer 2H-$MoTe_2$ film and promises potential applications of 2D materials in large-scale electronic and optoelectronic devices

Experimental Section

Synthesis of Large-Scale 2H-$MoTe_2$ Films: The $MoTe_2$ films were synthesized by tellurizing the Mo films at atmospheric pressure in a horizontal tube furnace equipped with mass flow controllers and a vacuum pump. Mo films were deposited on Si/SiO_2 substrates by magnetron sputtering. The substrates and Te powders were placed in an alumina boat, which was later inserted into a 1 inch diameter quartz tube inside the furnace. When the quartz tube was evacuated to less than 10 mTorr, high-purity Ar gas was let-in with a flow rate of 500 standard cubic centimeter per minute (sccm) until atmospheric pressure was reached. This process was repeated for three times. After that, the Ar flow rate was set to be 4 sccm, and high-purity H_2 gas was let-in with a flow rate of 5 sccm. The growth temperature and time were 650 °C and 2 h, respectively. Finally, the furnace was cooled down to room temperature naturally.

Transfer of the $MoTe_2$ Film onto Mesh Copper Grid: First, a droplet of isopropanol (IPA) was dropped on the $MoTe_2$ thin film synthesized on a Si/SiO_2 substrate. Then, a mesh copper grid was carefully put onto the IPA solution. After the IPA evaporated naturally, the copper grid adhered to the $MoTe_2$ film on the substrate. Then, a small amount of the dilute hydrofluoric (HF) solution (1.5%) was dropped on the substrate. After a few seconds, the copper grid together with the $MoTe_2$ film was detached from the substrate. Finally, the sample was thoroughly rinsed by deionized water.

Microscopic Confocal Raman Spectroscopy for Characterizing the $MoTe_2$ Film: Raman spectra of the $MoTe_2$ film were acquired by a Raman system (WITec alpha300). The microscope is equipped with an XYZ piezo-scan stage, which enables automatic scanning of the sample. A 50× objective lens (0.55 NA, Zeiss) was used to focus 532 nm laser onto the sample. Raman signals were detected by a spectrometer with 1800 g mm^{-1} grating coupled with a charged coupled device.

STEM Characterization: The HAADF-STEM images were acquired using a Nion U-HERMES 200 microscope with both monochromator and the aberration corrector operating at 60 kV. From the low-magnification HAADF-STEM image (Figure S9a, Supporting Information), a lower contrast with the interface could be observed. Along with the interface, some dark holes (the area with thinner 2H-$MoTe_2$) were occasionally observed, might be due to the insufficient supply of Mo atoms at the interface. Then, one such darker area was used to locate the interface and zoomed in to have a high-magnification view of the repaired interface (Figure S9b, Supporting Information).

Device Fabrication for Electrical Measurement: First, markers to locate the repair interfaces of the devices were defined using photolithography when the windows were opened which cover the damaged area. Then, a spatially controlled photolithography was needed to define the 2H

$MoTe_2$ channels at the repaired interface. The exposed $MoTe_2$ films were etched by RIE using O_2 and SF_6. The electrodes (10/50 nm Pd/Au) with distances of 10 μm were fabricated on three different regions (the original region, the repaired region, and the cross-interface region) using another spatial-controlled photolithography and e-beam evaporation processes.

Supporting Information

Supporting Information is available from the Wiley Online Library or from the author.

Acknowledgements

This work was supported by the National Natural Science Foundation of China (Nos. 61874003, 61521004, 51672007, and 11974023), Key Research Program of Frontier Sciences, CAS (Grant No. ZDBS-LY-JSC015), the Beijing Natural Science Foundation (No. 4182028), and the National Key R&D Program of China (Grant No. 2018YFA0306900). Key-Area Research and Development Program of GuangDong Province (Nos. 2018B030327001 and 2018B010109009). The authors acknowledge Electron Microscopy Laboratory at Peking University for the use of a Cs corrected electron microscope.

Conflict of Interest

The authors declare no conflict of interest.

Keywords

1T'/2H interface, $MoTe_2$, phase transitions, precise repair, recrystallization

Received: January 11, 2020
Revised: March 26, 2020
Published online: April 24, 2020

[1] M. Buscema, D. J. Groenendijk, S. I. Blanter, G. A. Steele, H. S. J. van der Zant, A. Castellanos-Gomez, *Nano Lett.* **2014**, *14*, 3347.
[2] X. Xu, S. Liu, B. Han, Y. Han, K. Yuan, W. Xu, X. Yao, P. Li, S. Yang, W. Gong, D. A. Muller, P. Gao, Y. Ye, L. Dai, *Nano Lett.* **2019**, *19*, 6845.
[3] K. Kang, K.-H. Lee, Y. Han, H. Gao, S. Xie, D. A. Muller, J. Park, *Nature* **2017**, *550*, 229.
[4] Z. Lin, Y. Liu, U. Halim, M. Ding, Y. Liu, Y. Wang, C. Jia, P. Chen, X. Duan, C. Wang, F. Song, M. Li, C. Wan, Y. Huang, X. Duan, *Nature* **2018**, *562*, 254.
[5] D. Akinwande, N. Petrone, J. Hone, *Nat. Commun.* **2014**, *5*, 5678.
[6] Q. H. Wang, K. Kalantar-Zadeh, A. Kis, J. N. Coleman, M. S. Strano, *Nat. Nanotechnol.* **2012**, *7*, 699.
[7] K. F. Mak, K. He, J. Shan, T. F. Heinz, *Nat. Nanotechnol.* **2012**, *7*, 494.
[8] D. Xiao, G.-B. Liu, W. Feng, X. Xu, W. Yao, *Phys. Rev. Lett.* **2012**, *108*, 196802.
[9] Y. Cao, V. Fatemi, A. Demir, S. Fang, S. L. Tomarken, J. Y. Luo, J. D. Sanchez-Yamagishi, K. Watanabe, T. Taniguchi, E. Kaxiras, R. C. Ashoori, P. Jarillo-Herrero, *Nature* **2018**, *556*, 80.
[10] Y. Cao, V. Fatemi, S. Fang, K. Watanabe, T. Taniguchi, E. Kaxiras, P. Jarillo-Herrero, *Nature* **2018**, *556*, 43.
[11] C. Jin, E. C. Regan, A. Yan, M. Iqbal Bakti Utama, D. Wang, S. Zhao, Y. Qin, S. Yang, Z. Zheng, S. Shi, K. Watanabe, T. Taniguchi, S. Tongay, A. Zettl, F. Wang, *Nature* **2019**, *567*, 76.
[12] K.-A. N. Duerloo, Y. Li, E. J. Reed, *Nat. Commun.* **2014**, *5*, 4214.
[13] X. Xu, S. Chen, S. Liu, X. Cheng, W. Xu, P. Li, Y. Wan, S. Yang, W. Gong, K. Yuan, P. Gao, Y. Ye, L. Dai, *J. Am. Chem. Soc.* **2019**, *141*, 2128.
[14] N. R. Pradhan, D. Rhodes, S. Feng, Y. Xin, S. Memaran, B.-H. Moon, H. Terrones, M. Terrones, L. Balicas, *ACS Nano* **2014**, *8*, 5911.
[15] N. Flöry, P. Ma, Y. Salamin, A. Emboras, T. Taniguchi, K. Watanabe, J. Leuthold, L. Novotny, *Nat. Nanotechnol.* **2020**, *15*, 118.
[16] D. Rhodes, S. H. Chae, R. Ribeiro-Palau, J. Hone, *Nat. Mater.* **2019**, *18*, 541.
[17] W. S. Leong, H. Wang, J. Yeo, F. J. Martin-Martinez, A. Zubair, P.-C. Shen, Y. Mao, T. Palacios, M. J. Buehler, J.-Y. Hong, J. Kong, *Nat. Commun.* **2019**, *10*, 867.
[18] S. Bertolazzi, S. Bonacchi, G. Nan, A. Pershin, D. Beljonne, P. Samorì, *Adv. Mater.* **2017**, *29*, 1606760.
[19] Y. Shen, T. Xu, X. Tan, L. He, K. Yin, N. Wan, L. Sun, *Adv. Mater.* **2018**, *30*, 1705954.
[20] H. Ahn, Y.-C. Huang, C.-W. Lin, Y.-L. Chiu, E.-C. Lin, Y.-Y. Lai, Y.-H. Lee, *ACS Appl. Mater. Interfaces* **2018**, *10*, 29145.
[21] J. C. Park, S. J. Yun, H. Kim, J.-H. Park, S. H. Chae, S.-J. An, J.-G. Kim, S. M. Kim, K. K. Kim, Y. H. Lee, *ACS Nano* **2015**, *9*, 6548.
[22] Y. Yoo, Z. P. DeGregorio, Y. Su, S. J. Koester, J. E. Johns, *Adv. Mater.* **2017**, *29*, 1605461.
[23] L. Zhou, K. Xu, A. Zubair, A. D. Liao, W. Fang, F. Ouyang, Y.-H. Lee, K. Ueno, R. Saito, T. Palacios, J. Kong, M. S. Dresselhaus, *J. Am. Chem. Soc.* **2015**, *137*, 11892.
[24] M. Yamamoto, S. T. Wang, M. Ni, Y.-F. Lin, S.-L. Li, S. Aikawa, W.-B. Jian, K. Ueno, K. Wakabayashi, K. Tsukagoshi, *ACS Nano* **2014**, *8*, 3895.
[25] D. H. Keum, S. Cho, J. H. Kim, D.-H. Choe, H.-J. Sung, M. Kan, H. Kang, J.-Y. Hwang, S. W. Kim, H. Yang, K. J. Chang, Y. H. Lee, *Nat. Phys.* **2015**, *11*, 482.
[26] C. H. Naylor, W. M. Parkin, J. Ping, Z. Gao, Y. R. Zhou, Y. Kim, F. Streller, R. W. Carpick, A. M. Rappe, M. Drndić, J. M. Kikkawa, A. T. C. Johnson, *Nano Lett.* **2016**, *16*, 4297.
[27] X. Ma, P. Guo, C. Yi, Q. Yu, A. Zhang, J. Ji, Y. Tian, F. Jin, Y. Wang, K. Liu, T. Xia, Y. Shi, Q. Zhang, *Phys. Rev. B* **2016**, *94*, 214105.
[28] Q. Song, H. Wang, X. Pan, X. Xu, Y. Wang, Y. Li, F. Song, X. Wan, Y. Ye, L. Dai, *Sci. Rep.* **2017**, *7*, 1758.
[29] J. H. Sung, H. Heo, S. Si, Y. H. Kim, H. R. Noh, K. Song, J. Kim, C. S. Lee, S. Y. Seo, D. H. Kim, H. K. Kim, H. W. Yeom, T. H. Kim, S. Y. Choi, J. S. Kim, M. H. Jo, *Nat. Nanotechnol.* **2017**, *12*, 1064.
[30] R. Ma, H. Zhang, Y. Yoo, Z. P. Degregorio, L. Jin, P. Golani, J. Ghasemi Azadani, T. Low, J. E. Johns, L. A. Bendersky, A. V. Davydov, S. J. Koester, *ACS Nano* **2019**, *13*, 8035.
[31] L. Liu, J. Wu, L. Wu, M. Ye, X. Liu, Q. Wang, S. Hou, P. Lu, L. Sun, J. Zheng, L. Xing, L. Gu, X. Jiang, L. Xie, L. Jiao, *Nat. Mater.* **2018**, *17*, 1108.